Analytica Chimica Acta 1422 (2026) 346110

Contents lists available at ScienceDirect

Analytica Chimica Acta

journal homepage: www.elsevier.com/locate/aca

Small molecules dually targeting SARS-CoV-2 and host G-quadruplexes: binding mechanism explored by integrated experiments and computations

Long-yu Zhu [a], Min Zhu [a], Lu-yan An [a], Jun-qin Qiao [a,*], Wei-juan Zheng [b], Ju-wen Shen [c], Li Mao [d], Hong-zhen Lian [a,**]

[a] State Key Laboratory of Analytical Chemistry for Life Science, School of Chemistry and Centre for Shared Scientific Research Facilities, Nanjing University, 163 Xianlin Avenue, Nanjing, 210023, China
[b] State Key Laboratory of Pharmaceutical Biotechnology, School of Life Sciences, Nanjing University, 163 Xianlin Avenue, Nanjing, 210023, China
[c] Shanghai Key Laboratory of Regulatory Biology, Institute of Biomedical Sciences and School of Life Sciences, East China Normal University, 500 Dongchuan Road, Shanghai, 200241, China
[d] Ministry of Education (MOE) Key Laboratory of Modern Toxicology, School of Public Health, Nanjing Medical University, 101 Longmian Road, Nanjing, 211166, China

HIGHLIGHTS

- Establish integrated experimental-computational framework for G4-ligand analysis.
- Simultaneously target the virus and host G-quadruplexes of SARS-CoV-2.
- Elucidation of distinct binding mechanisms between ligands and viral/host G4s.
- Provide guidance for designing G4-targeting ligands against SARS-CoV-2 infection.

GRAPHICAL ABSTRACT

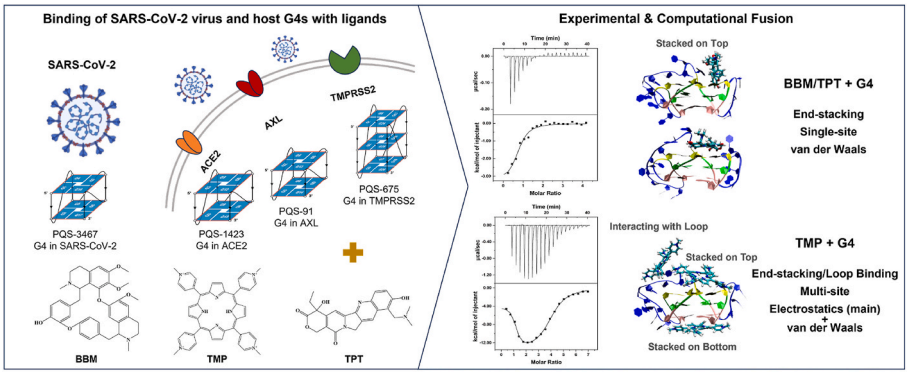

ARTICLE INFO

Handling Editor: Prof. De-Ming Kong

Keywords:
G-quadruplex (G4)
SARS-CoV-2
Small molecule ligands
Dual-targeting
Binding mechanism

ABSTRACT

Background: The ongoing COVID-19 pandemic caused by SARS-CoV-2 continues to pose significant challenges to global public health. Small-molecule ligands targeting G-quadruplex (G4) structures have shown considerable potential in antiviral therapy. However, existing studies have largely focused on individual viruses or isolated host systems, primarily employing in vitro or in vivo approaches to examine interactions between specific ligands and particular G4 structures. There remains a need for novel intervention strategies and a deeper mechanistic understanding of G4-ligand interactions to advance rational drug design.
Results: This study proposes, for the first time, a dual-targeting strategy that simultaneously engages G4 structures in both the SARS-CoV-2 viral genome and host genes relevant to viral entry (ACE2, AXL, and TMPRSS2). Four potential G4-forming sequences from these targets were experimentally confirmed to fold into stable RNA

* Corresponding author.
** Corresponding author.
E-mail addresses: qiaojunqin@nju.edu.cn (J.-q. Qiao), hzlian@nju.edu.cn (H.-z. Lian).

https://doi.org/10.1016/j.aca.2026.346110
Received 9 July 2026; Received in revised form 12 August 2026; Accepted 12 August 2026
Available online 12 August 2026

G4 structures. Using an integrated approach of spectroscopic analysis, isothermal titration calorimetry (ITC), and molecular dynamics (MD) simulations, we systematically evaluated the binding of three small-molecule ligands, berbamine (BBM), TMPyP4 (TMP), and topotecan (TPT), to the G4s. Among them, TMP demonstrated superior G4-stabilizing capability and significantly higher binding affinity compared to BBM and TPT. Energy decomposition analysis revealed that strong electrostatic interactions contributed by the positively charged pyridine groups of TMP are critical for stable binding. These results suggest that incorporating charged functional groups into ligand scaffolds can enhance G4-binding affinity.

Significance: By integrating comprehensive experimental characterization and molecular dynamics simulations to explore dual-targeting G4-ligand interactions, this work establishes a systematic methodology for in vitro G4-ligand research and provides critical insights for designing new SARS-CoV-2 therapeutics. This strategy holds significant potential not only against COVID-19 but also as a proactive blueprint for addressing future emerging viral threats.

1. Introduction

G-quadruplex (G4), a non-classical nucleic acid secondary structure, is formed by the stacking G-quartets through Hoogsteen hydrogen bonds in DNA or RNA sequences rich in tandem repeated guanine (G) [1]. G4 structures are widely present in the genomes of various organisms. They are involved in regulating gene expression, and play a crucial role in the life cycle of viruses. The formation of G4 structures in HIV-1 long terminal repeat promoter has been shown to reduce viral transcription [2]. G4s present in the host genome can also affect viral replication and entry, thereby influencing the infectivity and pathogenicity of the virus. Given this crucial role, research shows that small molecule ligands can specifically target G4s, displaying therapeutic potential for various diseases [3–6]. Benzoselenoxanthenes are used to inhibit the propagation of Influenza A virus by stabilizing the G4 structure in the host transmembrane serine protease 2 (TMPRSS2) gene, leading to down-regulation of TMPRSS2 expression [7]. Therefore, G4s have attracted attention as a potential therapeutic target for antiviral research.

The COVID-19 pandemic, caused by the SARS-CoV-2 virus, has been global public health crisis since its outbreak at the end of 2019. SARS-CoV-2 is a single-stranded RNA virus [8]. Sequence analysis using bioinformatics tools G4CatchAll, pqsfinder, and QGRS Mapper revealed the presence of multiple highly conserved potential G4-forming sequences (PQSs) in the SARS-CoV-2 genome [9–13]. Study showed that the RG-1 sequence located in the coding region of the N protein is capable of forming a G4 structure. Stabilization of RG-1 using PDP interferes with the translation of the nucleocapsid protein, thereby reducing the viral load [14]. SARS-CoV-2 infection also involves a variety of host cells, among which, angiotensin-converting enzyme 2 (ACE2), AXL receptor tyrosine kinase (AXL), and TMPRSS2 are important hosts during SARS-CoV-2 infection [15,16]. Liu et al. found that stabilizing the G4 mRNA in TMPRSS2 genome could inhibit the translation and protein expression of TMPRSS2, thus blocking the replication of SARS-CoV-2 [17]. This finding, along with other studies, strongly suggests that RNA G4s play an important role in the infection process of SARS-CoV-2 [18–20]. Therefore, the specific targeting of G4s in SARS-CoV-2 by small-molecule ligands could represent a promising therapeutic approach for the treatment of COVID-19.

G4-targeting small molecules are generally classified as synthetic molecules and natural products [21,22]. For instance, the synthetic porphyrin derivative TMPyP4, can effectively target G4s in SARS-CoV-2, thus inhibiting viral replication [23,24]. Additionally, studies have shown that both the semi-synthetic camptothecin derivative topotecan and the natural product of bis-benzylisoquinoline alkaloid berbamine could reduce the protein levels of RNA G4-containing host proteins, thereby preventing the entry of SARS-CoV-2 pseudovirus into target cells in the mouse model [25]. However, these studies primarily focused on in vivo and in vitro experiments to explore the interaction between a specific ligand with the G4 structures in individual viruses or in isolated hosts. This leaves an open question: can a single ligand simultaneously target both viral and host G4s to offer a more effective strategy for antiviral therapy? Importantly, previous work on HIV has provided a notable proof-of-concept. In that study, a designed ligand called NDI-MOC was shown to bind a viral G4, inhibit HIV-1 promoter activity, and also interfere with the host CXCR4 co-receptor, thereby impeding viral entry [26]. This finding offers evidence that a dual-targeting strategy, targeting both viral replication and entry, is feasible. Such simultaneous action can elicit a synergistic antiviral effect, which lays a solid foundation for developing dual-targeting antiviral strategies. Accordingly, we propose that ligands capable of simultaneously targeting both viral and host G4s, may represent a more effective strategy for against COVID-19. To achieve this, a detailed mechanistic study of ligand-G4 interactions, coupled with a comparative analysis of binding patterns across different ligands, is essential for developing high-affinity dual-targeting agents.

Experimental data from in vitro and in vivo provide foundational data on the binding affinity between G4s and ligands [27]. In parallel, computational techniques, including molecular docking and molecular dynamic (MD) simulations, complement experimental results to gain insight into the mechanisms and enable the rational optimization of ligand [28,29]. The integration of experiments and computation will provide a multidimensional perspective on the binding behavior of G4s with ligands.

Based on the above considerations, TMPyP4 (hereafter referred to as TMP), topotecan and berbamine (referred to as TPT and BBM) were chosen as the representative dual targeting ligands in this study. Their molecular structures were depicted in Fig. 1 in alphabetical order. By using bioinformatics tools, biophysical techniques and MD simulation, four stable RNA G4s within genomes of SARS-COV-2 virus and its hosts were successfully identified, and their three-dimensional models were constructed. Subsequently, the binding ability and mechanism of interaction between distinct ligands with these RNA G4s were systematically investigated. This research aims to establish a comprehensive suite of in vitro assays and computational simulation approaches for G4-ligand binding, providing guidance for the screening and optimization of ligands targeting both virus and host G4s, thereby advancing the development of novel antiviral drugs against SARS-CoV-2.

2. Experimental section

2.1. Bioinformatics prediction methods

The reference genomes of SARS-CoV-2 and hosts ACE2, AXL, and TMPRSS2 were obtained from the NCBI Virus Database under the accession numbers NC_045512, NM_001371415.1, NM_021913.5, and NM_005656.4, respectively [30]. G4 Hunter, pqsfinder, and QGRS Mapper were used to search for PQSs among the reference genomes [31]. For G4 Hunter, the window size was set to 25, the threshold for the host genome was set to 1.2, and the threshold for the virus was set to 0.9. When using pqsfinder, the maximum length of the predicted PQSs was set to 50, the minimum score was set to 20, and the maximum allowed defects were 3. For QGRS Mapper, the maximum length of the predicted PQS was set to 30, the minimum number of G-quadruplex layers was set

to 2, and the length of the loop region was in the range of 0-36.

2.2. Oligonucleotides and ligands

The oligonucleotide sequences to be used were selected according to the predicted results, and the sequences used in the experiments were custom-synthesized by Nanjing GenScript Biotech Corporation (Nanjing, China) and purified by RNase-free HPLC. BBM (berbamine, CAS: 6078-17-7) was purchased from TargetMol (Shanghai, China), TMP (5,10,15,20-tetrakis(N-methyl-4-pyridyl)porphyrin, CAS: 36951-72-1) and TPT (topotecan, CAS: 119413-54-6) were purchased from MCE China (Shanghai, China).

2.3. G4s and ligands preparation

The synthesized oligonucleotides were dissolved in 10 mM K_2HPO_4/KH_2PO_4 phosphate buffer (pH 7.0) containing 100 mM KCl to prepare a 100 μM RNA stock solution, which was then diluted to the targeted concentration according to the experimental requirements. The diluted solution was heated at 95°C for 10 min and slowly cooled to room temperature. After cooling, the solution was stored at 4°C overnight, followed by being stored at −80°C before use. BBM, TMP, and TPT were separately dissolved using ultrapure water prepared as 10 mM stock solutions, which were then stored at −80°C until being used.

2.4. Circular dichroism

Circular dichroism (CD) measurements were performed using a Chirascan digital circular dichroism spectropolarimeter (Applied Photophysics Ltd., Leatherhead, UK) and a quartz cuvette with an optical path of 1 mm. The sampling interval was set to 0.5 s, the slit width was 1 nm, and the wavelength range of the measurement was 220-320 nm with a step size of 1 nm. The final CD spectra were obtained by averaging three independent measurements.

CD-melting experiments were performed at 265 nm over a temperature range of 20-95°C with a heating rate of 1 °C/min. The concentration of each individual RNA was 10 μM, and for G4-ligand mixtures, the concentrations of the G4 and the ligand were both set to 10 μM.

2.5. Fluorescence spectroscopy

Fluorescence spectroscopy (FS) was measured using an F-7000 fluorescence spectrometer (Hitachi, Tokyo, Japan) at room temperature. The excitation wavelength was set at 260 nm. The excitation slit width was 10.0 nm and the emission slit width was 5.0 nm. The emission spectra were recorded at wavelength range of 300-480 nm, with a scanning rate of 1200 nm/min. The concentration of the RNA samples used for FS measurements was 10 μM.

2.6. Ultraviolet absorption spectroscopy

Ultraviolet (UV) absorption measurements were performed using a UH5300 UV-vis spectrophotometer (Hitachi, Tokyo, Japan) and a quartz cuvette with an optical path of 1 cm. The absorbance of the samples was tested across the wavelength range of 220-320 nm at room temperature. For the UV spectrum of G4-ligand mixtures, the concentrations of G4 and ligand were both set at 2 μM.

For isothermal difference spectrum (IDS) experiments, the initial spectra of RNA samples were recorded at room temperature in the absence of any stabilizing cation. Then KCl was added to the quartz cuvette to reach a final concentration of 100 mM, and the second spectrum was recorded after equilibration for 15 min. The IDS spectrum was calculated as the arithmetic difference between the initial spectrum (absence of KCl) and final (presence of KCl) spectrum after correction for dilution. The tested wavelength range was 220-320 nm, and the concentration of the RNA samples for IDS was 2 μM.

2.7. Nuclear magnetic resonance spectroscopy

The nuclear magnetic resonance (NMR) spectra were acquired on a Bruker Avance III HD 600 NMR spectrometer (Bruker, Fallanden, Switzerland) with water suppression using the pre-saturation method of the NOE effect. The pulse sequence was a 1D version of NOESY-PR1D. Chemical shifts (δ) were measured in ppm. RNA samples were dissolved in 10 mM K_2HPO_4/KH_2PO_4 buffer (pH 7.0) containing 100 mM KCl and 20% (*v/v*) D_2O, with a final concentration of 1 mM.

2.8. Isothermal titration calorimetry

Isothermal titration calorimetry (ITC) tests were performed using a MicroCal iTC200 (GE Healthcare, MA, USA) at 25°C. The ligand solution was titrated into the RNA solution at a rate of 2 μL each time with a titration interval of 120 s for 20 titrations and a stirring speed of 1000 rpm. The final titration results were fitted by the workstation software, iTC200 with Origin.

The concentrations of RNA G4s were 30 μM. For the assessment of binding interactions between G4s and BBM, and between G4s and TPT, the ligand concentration was maintained at 600 μM. When evaluating the binding between G4s and TMP, the ligand concentration was set to 1 mM for PQS-3467, PQS-1423, and PQS-675, whereas for PQS-91, the ligand concentration was adjusted to 600 μM. RNA and ligand samples were maintained in solution compatibility and both passed through a 0.22 μm filter before testing.

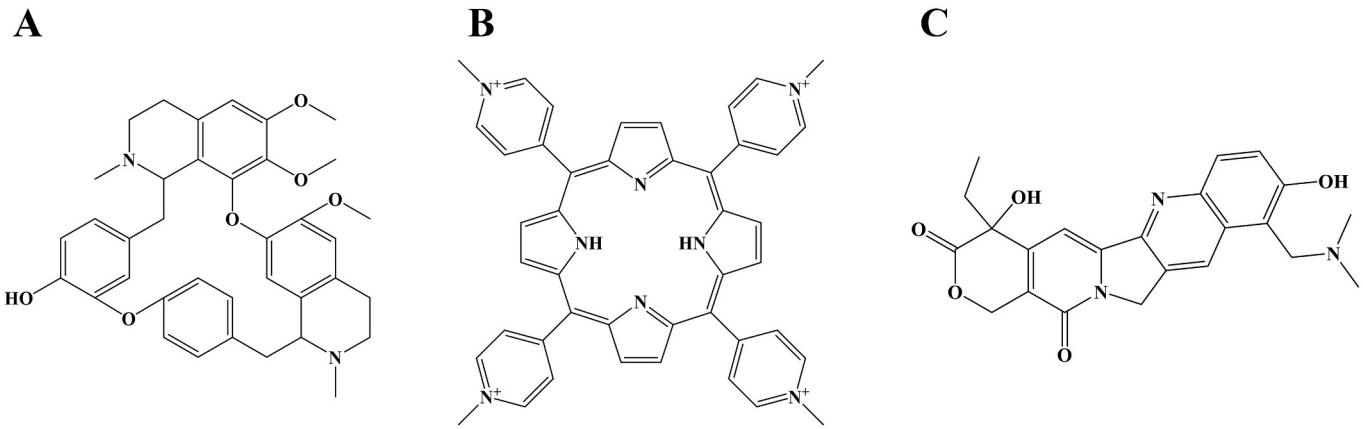

Fig. 1. Chemical structure of G4 ligands. (A) BBM; (B) TMP; (C) TPT.

2.9. Molecular modeling

The two-dimensional structures PQS-1423, PQS-91, and PQS-675 were predicted using RNAFold (http://rna.tbi.univie.ac.at/cgi-bin/RNAWebSuite/RNAfold.cgi) under 0.1 M salt concentration [32]. These predictions were then integrated with the topological features of the sequences obtained by CD experiments to construct the final structures using SimRNA (https://genesilico.pl/SimRNAweb) [33]. For PQS-3467, its three-dimensional structure was constructed using 3D-Nus (https://iith.ac.in/3dnus/Quadruplex.html) [34]. The above 3D structures were placed in a cubic water box utilizing the TIP3P water model, incorporating periodic boundary conditions and employing the amber14SB_OL5 force field [35]. The minimum distance between the G4 structure and the edge of the water box was set to 1 nm. To neutralize the whole system, 0.1 M KCl was added. A 500-step energy minimization was first performed using the conjugate gradient algorithm to ensure reasonable initial structures in terms of geometry and solvent orientation. This was followed by a 100 ps restrained kinetics to equilibrate the solvent and ions surrounding the RNA. Finally, a 400 ns MD simulation was conducted using GROMACS 2019 software under an NPT ensemble (T = 298.15 K, P = 1.0 atm) [36]. Temperature coupling was achieved through the V-rescale method, while pressure coupling as managed via the Parrinello-Rahman. The simulation results were visually analyzed using VMD 1.9.3 software [37].

2.10. Molecular docking and molecular dynamics simulations

The optimized G4 structures were initially preprocessed under the Protein Preparation Wizard module in Maestro 10.1 software, utilizing the OPLS_2005 force field [38,39]. The mol2 files of the three-dimensional structures of BBM, TMP, and TPT were downloaded from G4LDB (https://www.g4ldb.com) [40,41]. The three-dimensional structures of the three ligands were optimized under the Ligprep module using the OPLS_2005 force field. Subsequently, the ligands were docked to each of the four G4 structures by the Glide module in the Maestro program. The receptor grid box was created with G4 as the centroid, and the size of box was set to default value. Finally, the Glide Docking method was chosen to obtain the docking structure for subsequent analysis [42,43]. The position of the ligand relative to G4 obtained by the docking process was used as the initial position.

The force field of the ligands was parameterized by GAFF via Sobtop to obtain a reasonable template of the ligand molecule for subsequent kinetic simulations [44,45]. The system construction, simulation, and visualization of the complexes were carried out following the same protocol described above. The long-range electrostatic interactions and van der Waals interactions were handled by the Particle-Mesh Ewald (PME) method and a cutoff distance of 10 Å, respectively [46]. After energy minimization, a 100-ps pre-equilibration was performed. A 600 ns MD simulation was then carried out in the NPT ensemble at a temperature of 298.15 K using the V-rescale thermostat method with a time step of 2.0 fs.

The binding free energy between G4 and the ligand was analyzed using the Molecular Mechanics/Generalized Born surface area (MM/GBSA) method [47]. A total of 100 snapshots, extracted at 1 ns interval from the last stable 100 ns of each complex MD trajectory, were calculated using the gmx_MMPBSA tool [48,49].

3. Results and discussion

3.1. PQSs in the genome

The genomes of SARS-CoV-2, ACE2, AXL, and TMPRSS2 were searched for PQSs using three bioinformatics tools of G4 Hunter, pqsfinder, and QGRS Mapper. For the viral genome, the PQSs were selected based on predictions from G4 Hunter and the top three PQSs were predicted by QGRS Mapper. For the host genomes, the PQSs with high prediction scores and occurrence frequencies by each software were chosen. A total of 21 PQSs were selected and were detailed in Table S1. Subsequently, they were subjected to experiments to validate their ability to fold into G4s and structural stability.

3.2. Identification of G4 formation

CD spectroscopy was first employed to assess the G4 folding and conformations of annealed RNA samples, as depicted in Fig. S1. All PQSs exhibited varying levels of folding after annealing, evidenced by the spectral signatures. The negative signal near 240 nm and the positive signal near 265 nm for most of PQSs, indicated the presence of parallel G4s. Notably, the CD spectrum of PQS-2041 exhibited positive peaks around 265 nm and 290 nm and a negative peak at 240 nm, suggesting a hybrid G4 conformation. However, relying solely on CD was insufficient to conclusively confirm that these PQSs indeed formed G4 structures. This is because RNAs with stem-loop or hairpin structures have CD profiles similar to those of parallel G4s, which are characterized by a positive peak at 264 nm and a negative peak at 245 nm [50]. Therefore, additional characterization techniques were essential for comprehensive validation of G4 formation.

The intrinsic fluorescence of RNA will enhance as it folds into different secondary structures due to the stacking of the base planes. Specifically, for PQSs capable of forming G4s, a more pronounced fluorescence enhancement occurs compared to their single-stranded state [51]. The FS were recorded for both water-dissolved PQSs and PQSs annealed under K^+ condition, and the results were shown in Fig. S2. Notably, PQS-3467, PQS-1423, PQS-91, PQS-675, and PQS-2303 all exhibited substantial fluorescence enhancement, suggesting the formation of G4 structures for these five sequences.

Additionally, the G4 formation was further confirmed by monitoring the changes in UV absorbance before and after the addition of K^+, corresponding to the unfolded and folded states of PQSs, respectively. In UV, the hypochromic effect induced by the stacking of planes upon folding will result in a decreased absorbance at 295 nm for G4s compared to its unfolded state. As displayed in Fig. S3, the six sequences of PQS-3467, PQS-1423, PQS-91, PQS-675, PQS-1280, and PQS-2303 all exhibited a negative peak in IDS at 295 nm and two positive absorption peaks in the range of 220-290 nm, consistent with G4 folding.

Collectively, CD, FS, and IDS provide complementary evidence for G4 formation from three distinct perspectives, including topological conformation, conformational rigidity, and base stacking. This cross-validation supported the folding of five PQSs (PQS-3467, PQS-1423, PQS-91, PQS-675, and PQS-2303) into G4 structures. Among these, two (PQS-675 and PQS-2303) are located within the TMPRSS2 genome. PQS-675 is located within the open reading frame (ORF), whereas PQS-2303 resides in an untranslated region (UTR) [17]. Comparatively, PQS-675 is more highly conserved across vertebrates. Taking into account both the biophysical validation (CD, FS, and IDS) and genomic conservation, we selected PQS-3467, PQS-1423, PQS-91, and PQS-675 as representative G4 sequences in the SARS-CoV-2 virus and host genomes for subsequent studies. Their respective sequences were detailed in Table 1, and the corresponding CD, FS, and IDS spectra were shown in Fig. 2A–C.

NMR represents a classical and effective methodology for structural characterization of nucleic acid macromolecules. To obtain direct and definitive structural evidence on G4 formation, the four PQSs were

Table 1
PQS sequences studied in this work.

Name	Sequence
PQS-3467	5′-**gg**a**gg**a**gg**uguugca**gg**-3′
PQS-1423	5′-u**gg**a**gg**u**gg**au**gg**ucuuuaaagggga-3′
PQS-91	5′-g**ggg**g**gg**a**ggg**cc**ggg**-3′
PQS-675	5′-**ggg**c**ggg**cggccugca**ggg**acau**ggg**-3′

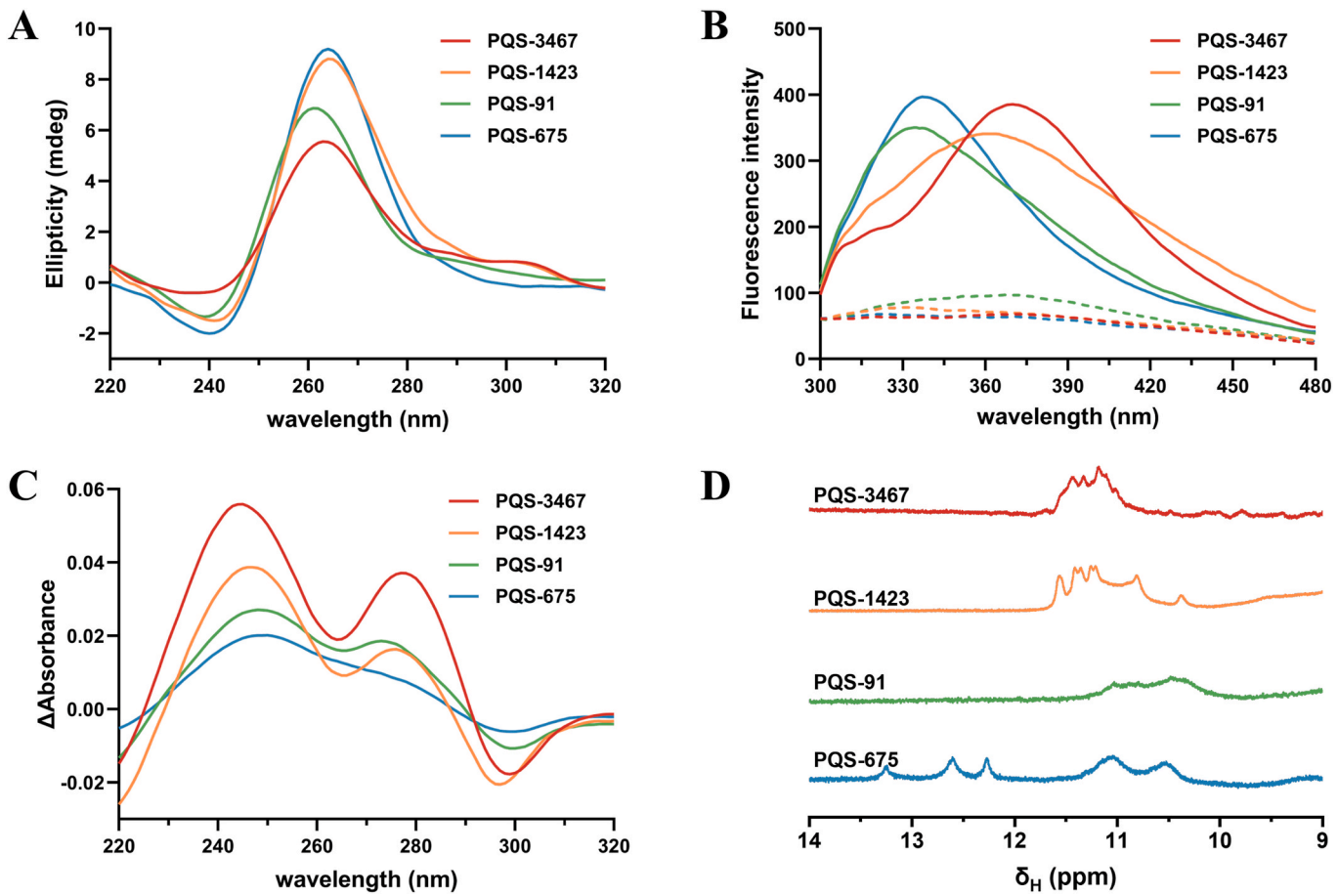

Fig. 2. Characterization of G4 formation using different spectroscopic techniques. (A) CD spectra of different PQSs annealed in 10 mM K_2HPO_4/KH_2PO_4 buffer containing 100 mM KCl. (B) FS spectra of different water-dissolved (dashed lines) or annealed PQSs (solid lines). (C) IDS spectra resultant from the difference of UV spectra in the presence and absence of KCl. (D) ^{1}H NMR spectroscopy of different PQSs. All measurements were performed at 25°C.

further characterized using 1D ^{1}H NMR (Fig. 2D). The characteristic imino proton resonances at 10-12 ppm clearly indicated the formation of stable G4 structures in solution. In summary, the integration of CD, FS, IDS, and NMR provided unambiguous evidence that all four selected PQSs can stably fold into parallel G4 conformations.

3.3. Spectroscopic characterization of ligands binding to G4s

The binding of ligands to G4s can perturb their local microenvironments, causing changes in the G4s structure, which is reflected in the variations of spectral signals. Therefore, CD measurements were conducted for the annealed PQS-3467, PQS-1423, PQS-91, and PQS-675 both before and after their equivalent binding with the ligands (Fig. S4).

The results showed that the signal intensity at 265 nm for all the G4s had somewhat changed, suggesting that the ligand had established a certain degree of interaction with the G4 structures. However, the initial topology of these G4s did not change, maintaining their parallel conformations. UV experiments revealed that the maximal UV absorption wavelength of G4s was around 254 nm. After interacting with ligands, the absorption peak did not shift, only the absorption intensity was affected. Among them, PQS-91 showed the most significant changes, as illustrated in Fig. S5. The CD and UV results demonstrated that all three ligands were capable of binding to these G4s. And the interaction between these ligands and G4s just influenced the stacking of the G-quartet planes, without inducing any conformational changes in the G4 structures.

3.4. The effects of ligands on the thermal stability of G4s

CD melting experiments were employed to evaluate the stabilizing effects of different ligands on G4s. This evaluation was conducted through the measurement of the change of T_m of G4s before and after ligand addition (Fig. S6). The ΔT_m value is defined as the difference between the T_m of the G4-ligand complex and that of the corresponding free G4. The results were summarized in Table S2. It could be observed that ligands BBM and TPT destabilized the G4s of PQS-3467, PQS-1423, and PQS-675, while ligand TMP effectively stabilized these G4s. In contrast, the T_m of PQS-91 remained undetectable (>95°C) both before and after the addition of ligands, indicating exceptional thermal stability. Further spectral analysis revealed that the addition of ligands did not result in a shift of characteristic CD peak of PQS-91, although there was a slight decrease in the signal intensity (Fig. S7). This confirmed that the ligands affect the planar stacking of the G-quartets in PQS-91 without altering its native G4 conformation. Notably, both the free G4 structures and G4-ligand complexes remained stable under physiological temperature.

3.5. Affinity testing of G4 with ligands

The ITC experiments allow for the determination of the stoichiometric ratio *n*, association constant K_a and dissociation constant K_D of G4s when they bind to different ligands through a series of titrations, as illustrated in Fig. 3. The values of *n*, K_a, and K_D of G4s with different ligands were presented in Table 2.

Both BBM and TPT exhibited a 1:1 binding ratio with PQS-3467,

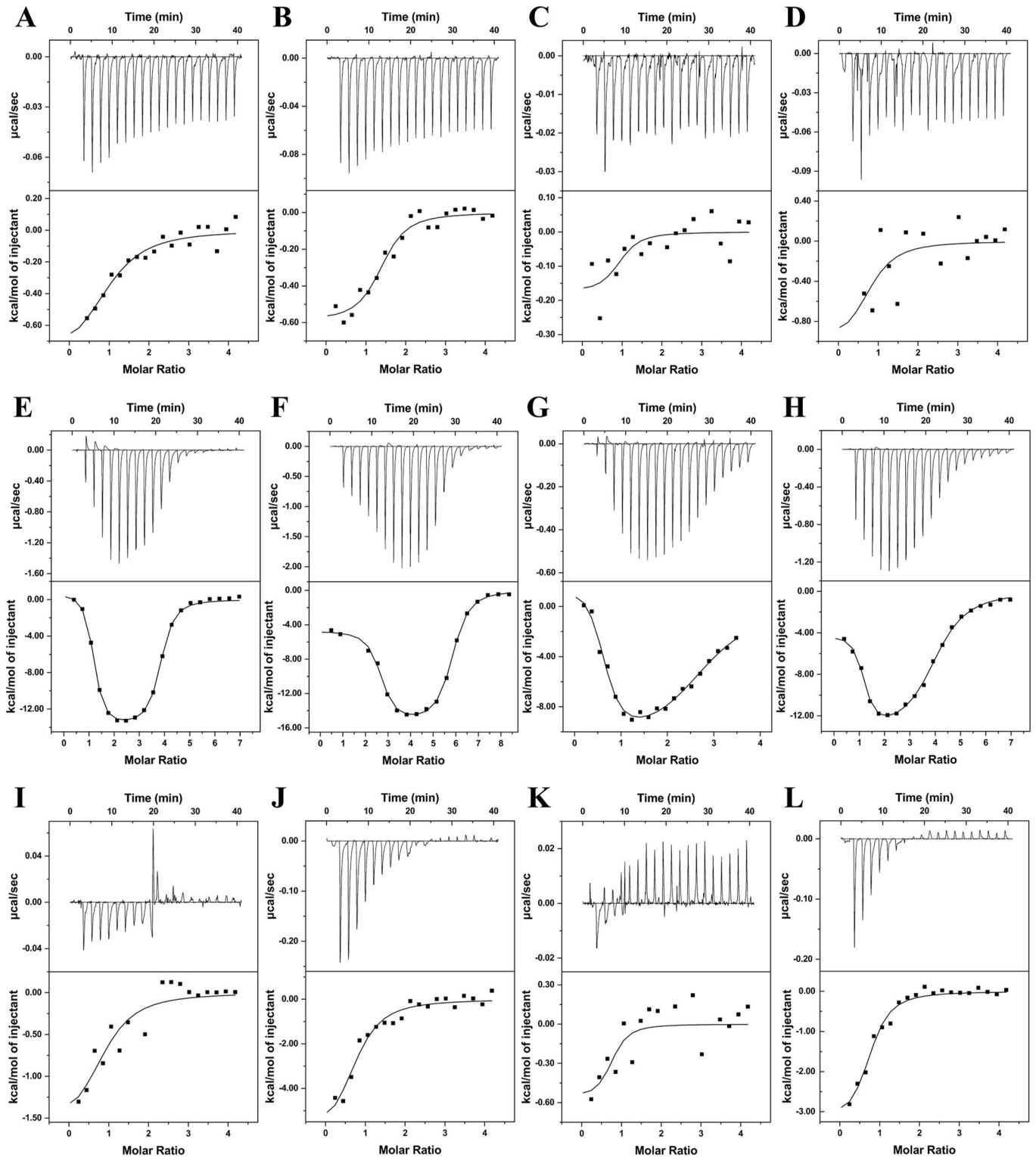

Fig. 3. Isothermal titration calorimetry curves of G4s and ligands. (A-D) PQS-3467, PQS-1423, PQS-91, and PQS-675 with BBM; (E-H) PQS-3467, PQS-1423, PQS-91, and PQS-675 with TMP; (I-L) PQS-3467, PQS-1423, PQS-91, and PQS-675 with TPT.

PQS-1423, PQS-91, and PQS-675. In contrast, TMP displayed a 3:1 binding ratio with PQS-3467, PQS-1423, and PQS-675, including one high-affinity site and two lower-affinity sites. The binding ratio of TMP to PQS-91 was 2:1, and the K_{D1} and K_{D2} value indicated the presence of one high-affinity site and one low-affinity site with the PQS-91 G4 structure for TMP binding.

The ITC results revealed that both BBM and TPT exhibited binding affinity with all four G4s at the micromolar level. Whereas for TMP, there were multiple binding sites with G4s. Notably, its interactions with PQS-3467, PQS-1423, and PQS-675 achieved nanomolar-level binding affinity at high-affinity sites. Comparatively, the affinity of TMP at its two binding sites for PQS-91 was lower.

Table 2
The different *n*, *Ka* and K_D of G4s with ligands BBM, TMP, and TPT.

Ligand	Values	PQS-3467	PQS-1423	PQS-91	PQS-675
BBM	n	1.03	1.37	0.911	0.800
	K_a	1.09×10^5 M^{-1}	4.39×10^5 M^{-1}	4.31×10^5 M^{-1}	1.91×10^5 M^{-1}
	K_D	9.17 μM	2.28 μM	2.32 μM	5.23 μM
TMP	n_1	1.04	2.49	0.596	1.05
	K_{a1}	1.02×10^8 M^{-1}	7.17×10^7 M^{-1}	6.19×10^6 M^{-1}	1.46×10^7 M^{-1}
	K_{D1}	9.80 nM	13.9 nM	162 nM	68.5 nM
	n_2	2.66	3.18	2.19	2.88
	K_{a2}	1.41×10^6 M^{-1}	9.03×10^5 M^{-1}	1.83×10^5 M^{-1}	2.27×10^5 M^{-1}
	K_{D2}	720 nM	1.11 μM	5.46 μM	4.41 μM
TPT	n	0.906	0.761	0.720	0.738
	K_a	1.38×10^5 M^{-1}	1.75×10^5 M^{-1}	5.38×10^5 M^{-1}	3.22×10^5 M^{-1}
	K_D	7.25 μM	5.71 μM	1.86 μM	3.11 μM

3.6. G4 structure construction and optimization

At present, there is lack of three-dimensional structural analysis of RNA G4 in SARS-CoV-2 related viruses and host genomes. To investigate the mechanisms of G4s binding with different ligands, we first constructed and optimized the RNA G4 structures. The initial structures of each G4 before optimization were presented in Fig. 4A–D. MD simulations of the constructed G4 systems were subsequently carried out in an aqueous solution environment over a period of 400 ns.

To analyze the stability of G4s, the RMSD of the systems were calculated, and the data were shown in Fig. S8. At the beginning of the simulation, obvious fluctuations in the RMSD of the four G4 systems. After approximately 100 ns, these systems generally reached an equilibrium state.

The structures of each G4 after simulation optimization were presented in Fig. 4E–H. The all-atom RMSD of PQS-1423 exhibited a jump near 200 ns. Observation of the trajectory and the RMSD of G-tetrads revealed that these fluctuations were caused by changes in the orientation of the bases in the loop region, while the G4 structure remained stable. In the initial model of PQS-3467, the loop region exhibited a relatively compact structure as in Fig. 4A. After a 50 ns of simulation, it tended to evolve into a looser and more irregular loop arrangement as shown in Fig. 4E. This looser loop configuration was maintained for the following 350 ns. The loops of PQS-91 and PQS-675 showed only slight variations at the beginning of the simulation, and the all-atom RMSD of both G4s stabilized around 4 Å in subsequent simulations. The RMSD of the G-tetrads in each G4 system reached a steady state after 50 ns, reflecting the stability of the formed G4 structures. Furthermore, the centers-of-mass (COM) distances between the G-tetrads of each G4 system remained stable over the simulated time frame (Fig. S8), suggesting the stability of the constructed G4 structures.

3.7. Structures of the complexes formed by G4s and ligands

The G4-ligand complex structures were obtained by determining the position of the ligand relative to G4s based on the molecular docking results (Fig. S9) and relevant literatures [52,53]. The pre-equilibrated structures were depicted in Fig. S10. Subsequently, a 600 ns molecular dynamics simulation was conducted, with resulting equilibrated structures illustrated in Fig. 5. The representative trajectory snapshots of different G4-ligand complexes and the corresponding analysis of the structural trajectory during the simulation process were displayed in the Supporting Information (Fig. S11–S33). RMSD indicated the stability of the complex systems, while the COM distance reflected the stability of the G-tetrads and the distance between G4 and the ligand, as detailed in Figs. S16, S22, S27, and S33.

The G4-ligand complex systems reached equilibrium within the simulated time frame. Analysis of the simulated complex structures revealed that both BBM and TPT ligands predominantly bound to the terminal plane of G4s, as presented in Fig. 5A–D and I-L. In contrast,

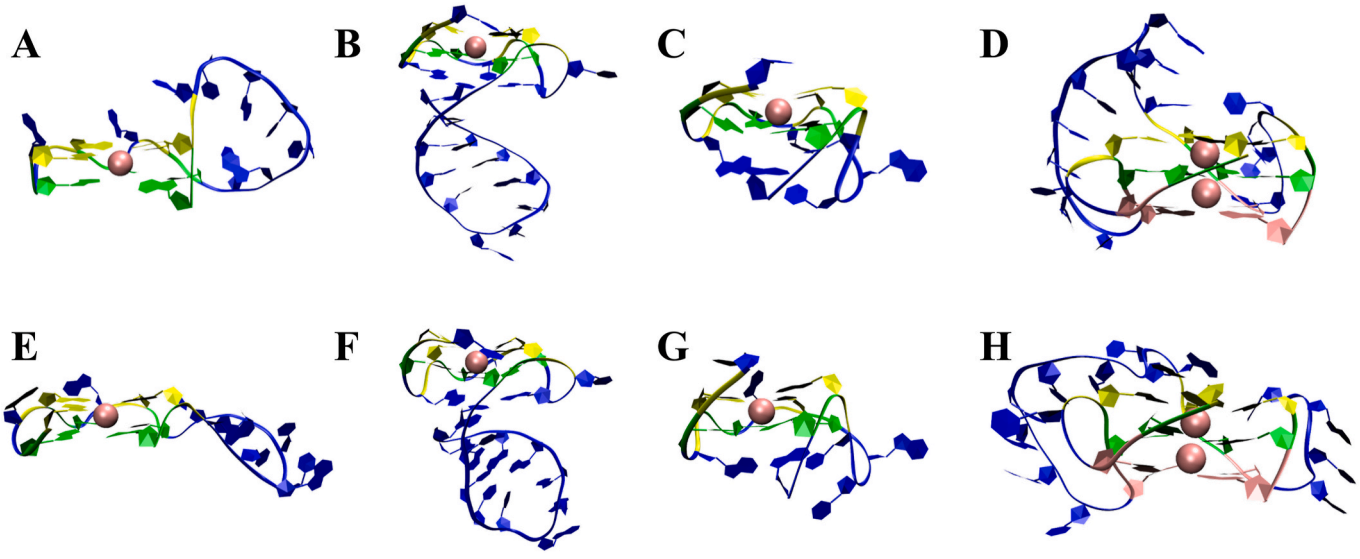

Fig. 4. The three-dimensional models of each PQS before and after dynamic optimization. (A) Initial PQS-3467; (B) Initial PQS-1423; (C) Initial PQS-91; (D) Initial PQS-675; (E) Optimized PQS-3467; (F) Optimized PQS-1423; (G) Optimized PQS-91; (H) Optimized PQS-675. The first G-quartet layer is represented in yellow, the second layer in green, and the third layer in pink. (For interpretation of the references to colour in this figure legend, the reader is referred to the Web version of this article.)

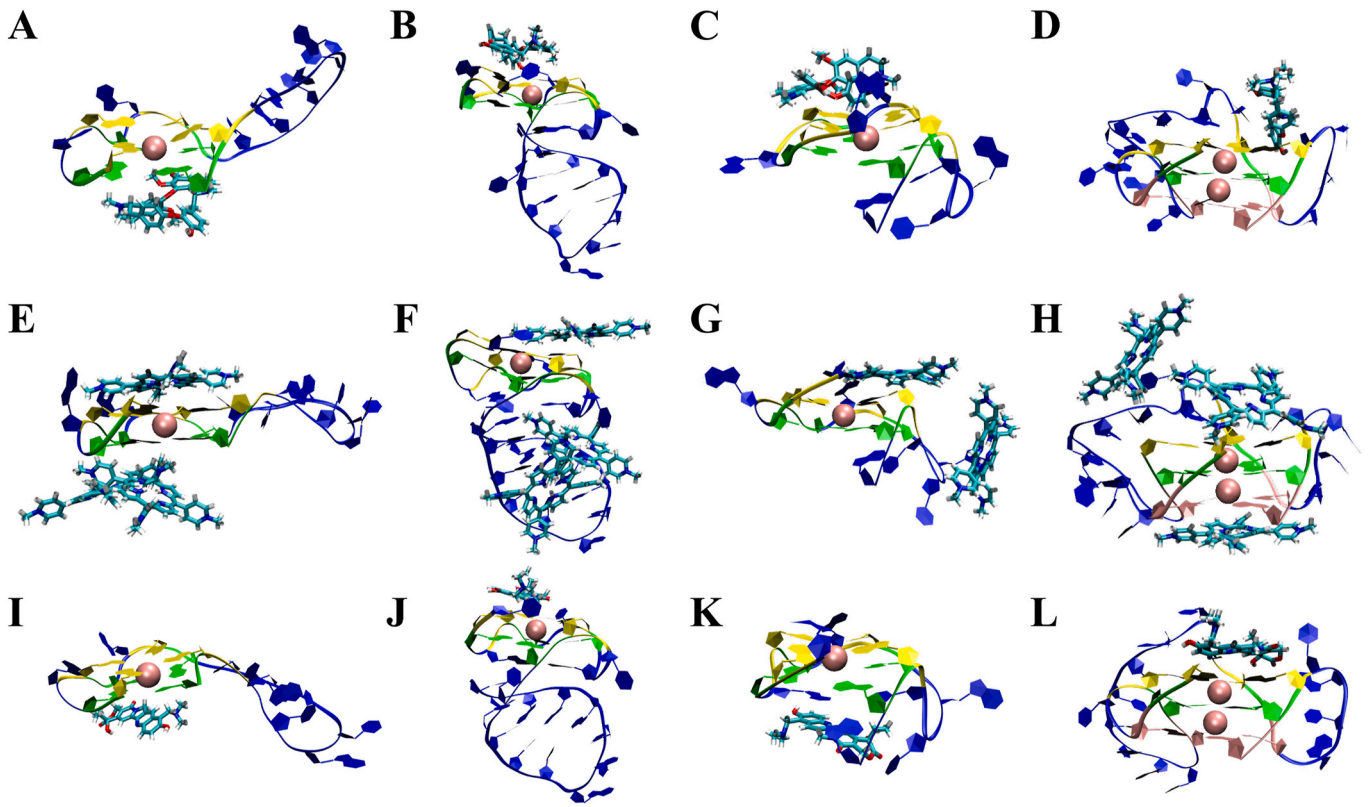

Fig. 5. The structure of the complexes formed by G4 and different ligands after dynamics simulations. (A-D) PQS-3467, PQS-1423, PQS-91, and PQS-675 with BBM; (E-H) PQS-3467, PQS-1423, PQS-91, and PQS-675 with TMPs, presented as superimposed images; (I-L) PQS-3467, PQS-1423, PQS-91, and PQS-675 with TPT. The first G-quartet layer is represented in yellow, the second layer in green, and the third layer in pink. (For interpretation of the references to colour in this figure legend, the reader is referred to the Web version of this article.)

TMP not only interacted with each G4 via terminal stacking, but also bound to the loop region and grooves. The presence of multiple binding sites for TMP within G4 structures was confirmed, a finding consistent with the ITC results. Subsequently, the binding energies between G4s and the ligands after equilibrium of the system were calculated and decomposed to elucidate the mechanisms of interaction.

3.8. Energy analysis of the binding between G4s and ligands

The energy analysis was performed using the last stable 100 ns of the dynamics simulation, with the results presented in Table 3. This analysis was employed to compare the binding energies and binding modes of the three ligands BBM, TPT and TMP toward G-quadruplex structures.

Upon reaching system equilibrium, the alkaloid derivatives BBM and TPT bound to the G4s by end-stacking, attributed to the aromatic rings in their structures. For the same G4, the binding energy contributions of

Table 3
The binding free energy of each system (kJ/mol).

Contribution[a]	ΔG_{vdW}	ΔG_{ele}	ΔG_{GB}	ΔG_{SA}	ΔG^{b}_{Total}
PQS-3467-BBM	−36.84 ± 0.26	−0.52 ± 0.07	2.17 ± 0.05	−3.17 ± 0.01	−38.35 ± 0.25
PQS-3467-TMP1	−29.67 ± 0.32	−151.66 ± 0.28	146.26 ± 0.26	−2.95 ± 0.03	−38.02 ± 0.34
PQS-3467-TMP2	−50.62 ± 0.33	−143.04 ± 0.33	139.96 ± 0.30	−3.87 ± 0.02	−57.57 ± 0.34
PQS-3467-TMP3	−27.57 ± 0.23	−138.24 ± 0.19	135.05 ± 0.18	−2.71 ± 0.01	−33.46 ± 0.22
PQS-3467-TPT	−35.82 ± 0.27	−1.98 ± 0.09	3.41 ± 0.07	−2.40 ± 0.02	−36.79 ± 0.26
PQS-1423-BBM	−40.15 ± 0.51	0.44 ± 0.11	1.00 ± 0.10	−3.21 ± 0.04	−41.93 ± 0.53
PQS-1423-TMP1	−31.43 ± 0.33	−251.78 ± 0.41	242.38 ± 0.38	−3.74 ± 0.04	−44.57 ± 0.35
PQS-1423-TMP2	−36.29 ± 0.27	−196.36 ± 0.33	191.26 ± 0.31	−2.78 ± 0.03	−44.16 ± 0.30
PQS-1423-TMP3	−23.34 ± 0.75	−233.60 ± 1.06	224.69 ± 0.99	−3.16 ± 0.09	−35.42 ± 0.87
PQS-1423-TPT	−43.90 ± 0.22	0.18 ± 0.09	1.43 ± 0.08	−2.47 ± 0.03	−44.75 ± 0.23
PQS-91-BBM	−40.84 ± 0.32	0.37 ± 0.06	1.15 ± 0.06	−3.01 ± 0.02	−42.33 ± 0.33
PQS-91-TMP1	−23.63 ± 0.17	−121.31 ± 0.27	118.25 ± 0.26	−2.25 ± 0.01	−28.74 ± 0.18
PQS-91-TMP2	−33.63 ± 0.37	−129.26 ± 0.32	126.01 ± 0.30	−2.57 ± 0.03	−39.45 ± 0.41
PQS-91-TPT	−39.63 ± 0.25	−1.27 ± 0.07	2.84 ± 0.06	−2.63 ± 0.01	−40.69 ± 0.25
PQS-675-BBM	−45.68 ± 0.36	1.48 ± 0.09	1.00 ± 0.07	−3.46 ± 0.02	−46.66 ± 0.35
PQS-675-TMP1	−30.39 ± 0.23	−200.36 ± 0.30	195.29 ± 0.28	−3.41 ± 0.02	−38.88 ± 0.24
PQS-675-TMP2	−51.92 ± 0.19	−230.64 ± 0.32	223.47 ± 0.28	−3.67 ± 0.02	−62.76 ± 0.21
PQS-675-TMP3	−37.60 ± 0.40	−202.18 ± 0.40	196.71 ± 0.37	−3.08 ± 0.03	−46.15 ± 0.44
PQS-675-TPT	−41.15 ± 0.26	2.03 ± 0.07	−0.28 ± 0.06	−2.32 ± 0.02	−41.73 ± 0.27

a: Mean ± standard errors (SE); b: $\Delta G_{Total} = \Delta G_{vdW} + \Delta G_{ele} + \Delta G_{GB} + \Delta G_{SA}$.

BBM and TPT showed no statistically significant difference. van der Waals interactions emerged as the predominant energetic contributor to complex stabilization. Specifically, the binding free energy of PQS-3467 with BBM is −38.35 ± 0.25 kJ/mol, and van der Waals interactions provide a major contribution of −36.84 ± 0.26 kJ/mol. Similarly, the binding free energy of PQS-3467 with TPT is −36.79 ± 0.26 kJ/mol, with van der Waals interactions contributing −35.82 ± 0.27 kJ/mol.

In contrast, the binding profile of TMP is governed by a different mechanism. The positively charged N-methyl-4-pyridyl groups together with the planar porphyrin group enable TMP to interact with G4s through electrostatic attraction and end-stacking. Accordingly, the energy analysis indicated that the electrostatic interactions were the primary contributor to the binding energy between TMP and G4s, although van der Waals interaction also contributed significantly to the energy. For instance, the total binding free energy of PQS-1423-TMP complex via end-stacking (PQS-1423-TMP1) is −44.57 ± 0.35 kJ/mol, with a van der Waals contribution of −31.43 ± 0.33 kJ/mol and a prominent electrostatic contribution of −251.78 ± 0.41 kJ/mol. Comparable energetic profiles were observed for the loop-binding mode, as illustrated by the binding energy of PQS-1423-TMP2 listed in Table 3.

Furthermore, energy decomposition characterized the binding sites formed by key contributing bases and quantified their energy contributions to G4-ligand binding (Fig. 6). In contrast, the corresponding analysis restricted to ligand contribution was presented in Fig. S34. Given that BBM and TPT mainly bind to G4s via single-site end-stacking interactions, we focused on a detailed analysis of the multiple binding sites of TMP on different G4 structures.

Notably, there was a high-affinity site for TMP binding at PQS-3467, specifically at the 5′ terminal G-tetrad plane, which is constituted by G1, G4, G7 and G16, as illustrated in Fig. 6A–B. While the G-tetrad plane at 3′ terminal end (G2, G4 and G5) demonstrated a significantly lower free energy than that at the 5′ terminal plane, which can be attributed to the reduced number of bases involved in TMP binding. For TMP bound in the loop region, it showed a stronger tendency to approach the 3′ terminal plane when simulation achieved equilibrium, as shown in Fig. S14, but at a lower energy compared to fully stacked on the plane. Structural superposition revealed that after stacking on the 3′ terminal plane, there was spatial hindrance when the third TMP ligand tried to bind with PQS-3467. This observation also corroborated the ITC results that the binding ratio of TMP to PQS-3467 was between 2 and 3.

For PQS-1423, the 5′ terminal plane formed by G2, G5, G8 and G12 and the groove in the loop region near the 3′ end constructed by A10, A21, G22, G23, G24 and G25 provided two sites with very close affinity for TMP binding (Table 3, Fig. 6C–D). While the binding free energy of the third site in the loop region formed by U16, U17, A21 and G22 was slightly lower than that of the first two sites.

Upon superimposing the three TMP binding states, from Fig. 5F, we could find that there were no steric hindrance effects among the sites in PQS-1423. It indicated that the two slightly higher energy sites with close affinities cooperatively stabilized the G4 binding and formed a stable complex, facilitating the binding of the third TMP with PQS-1423. This observation was also consistent with the stoichiometric ratios determined by ITC.

The free energy of TMP bound to PQS-91 at 5′ terminal plane showed a weaker affinity compared to other G4s. At a 1:1 ratio, complete binding might not be fully achieved, as reflected in the ITC result, where the stoichiometric ratio for the first site was 0.596, and the affinity K_{D1} was 162 nM. The other TMP binding site was dynamic, shifting from the 3′ terminal plane of PQS-91 during the kinetic process to a loop region (G10, C11 and C12, Fig. 6E–F) at equilibrium, suggesting that a binding preference to the loop despite its lower affinity.

The 3′ terminal plane (G3, G7, G19 and G26) of PQS-675 presented a high-affinity site for TMP (Fig. 6G–H), which was attributed to the absence of steric hindrance from loop regions. The other two sites were located at the 5′ terminal plane (G1, G14 and G24) and the loop region (C11, C12, U13, G14 and C15), respectively, exhibiting comparable binding affinities that were both weaker than that of the 3′ terminal plane. Structural superposition revealed that the three sites on PQS-675 had no obvious spatial hindrance, enabling effective binding with TMP, as corroborated by ITC results.

From the binding energy analysis as well as the ITC results, it could be seen that the porphyrin scaffold, when combined with positively charged N-methyl-4-pyridyl substituents, provides TMP with diverse recognition sites. This structure allows TMP to more effectively target the G4s in both the SARS-CoV-2 virus and the host genome. Remarkably, the cationic groups play a pivotal role in this enhanced binding capability.

The high affinity of TMP for G4s highlights its potent targeting capability. However, as a first-generation ligand, TMP may also interact with canonical duplex DNA and other nucleic acid conformations via non-specific electrostatic contacts. However, our binding data indicate that the TMP–G4 interaction is not exclusively charge-driven. TMP displays differential affinity across distinct G4 topologies and even among binding sites within the same G4, suggesting that shape complementarity and specific base interactions substantially modulate binding strength in concert with electrostatics. This observation informs a strategy for future optimization: affinity can be maintained through cationic groups, while selectivity can be enhanced by optimizing the spatial arrangement of substituents to achieve better topological matching with target G4s, as exemplified by ethoxy-linked N-methylpyridyl porphyrins that retain electrostatic attraction while disfavoring duplex intercalation [54].

4. Conclusions

Highly conserved G-quadruplexes (G4s) in the SARS-CoV-2 genome and its key host genes are significant functional elements during viral infection. In this pioneering study, we systematically characterized the binding profiles and molecular mechanisms of three ligands (BBM, TMP, and TPT) interacting with G4s from both viral and host sources for the first time. Our results revealed that the naturally derived broad-spectrum compounds BBM and TPT bind weakly to both viral and host G4s, with van der Waals forces as the dominant interaction mode. In contrast, synthetic compound TMP exhibits high affinity for G4s with electrostatic interactions as the main energetic component. These observations suggest that modification of ligands to increase their contribution to electrostatic interactions with G4s can potentially improve both binding affinity and multi-site binding capabilities. To improve selectivity, we propose optimizing spatial conformation and strengthening loop-region specific interactions. Our work has established a comprehensive experimental and computational framework for characterizing G4-ligand interactions. Beyond enriching the landscape of G4-targeted anti-SARS-CoV-2 research, this work provides mechanistic insights that can guide rational ligand design and optimization, and ultimately accelerate the development of next-generation antiviral therapeutics.

CRediT authorship contribution statement

Long-yu Zhu: Data curation, Formal analysis, Investigation, Methodology, Validation, Visualization, Writing – original draft. **Min Zhu:** Investigation, Methodology. **Lu-yan An:** Investigation, Methodology. **Jun-qin Qiao:** Formal analysis, Funding acquisition, Project administration, Resources, Validation, Writing – review & editing. **Wei-juan Zheng:** Conceptualization, Investigation, Supervision. **Ju-wen Shen:** Software. **Li Mao:** Investigation, Supervision. **Hong-zhen Lian:** Conceptualization, Funding acquisition, Resources, Supervision, Writing – review & editing.

Funding

This work was supported by the National Natural Science Foundation

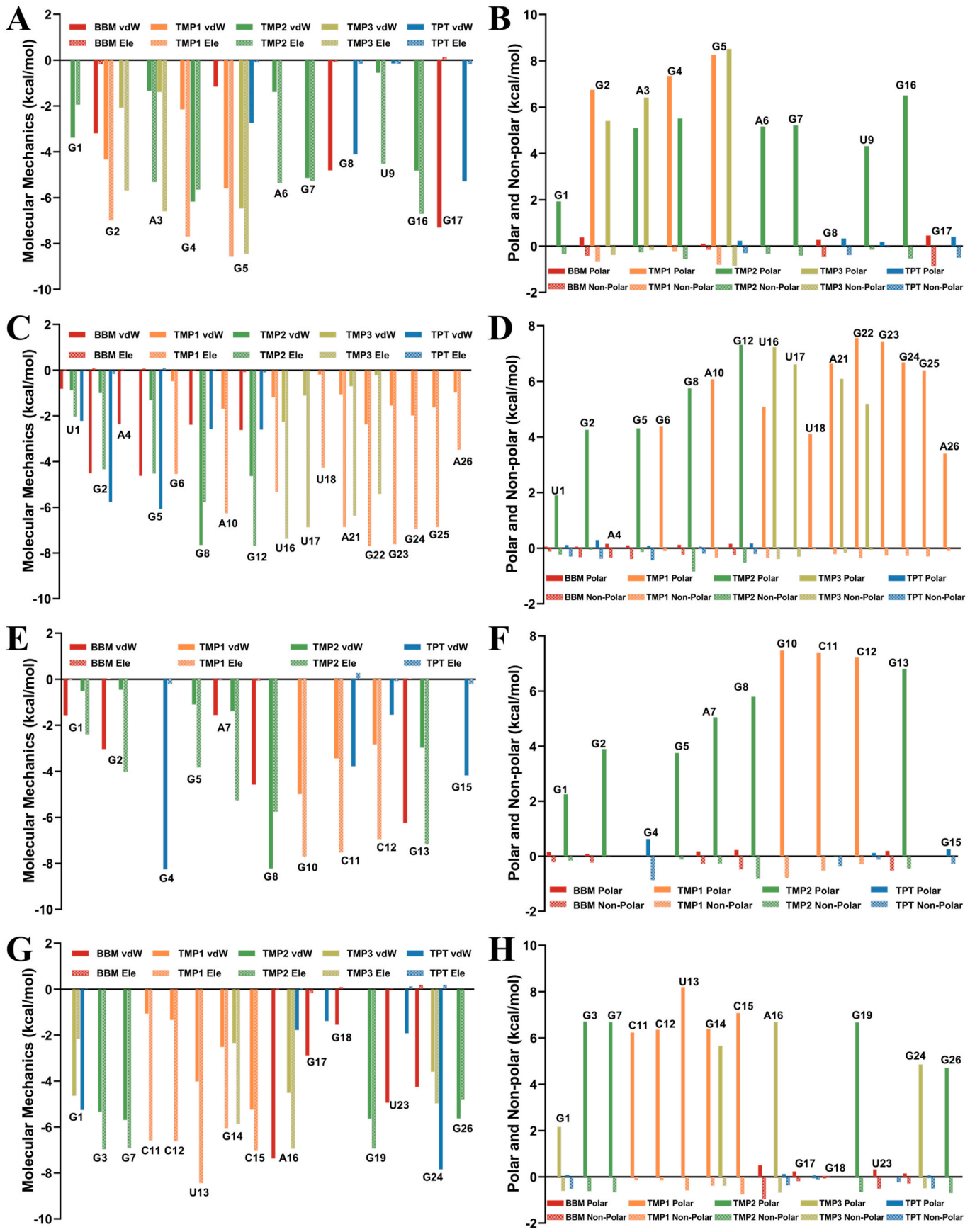

Fig. 6. Energy decomposition diagrams of G4s when bound to ligands. (A-B) Molecular mechanics and solvation energy terms for the binding of PQS-3467 to ligands; (C-D) Molecular mechanics and solvation energy terms for the binding of PQS-1423 to ligands; (E-F) Molecular mechanics and solvation energy terms for the binding of PQS-91 to ligands; (G-H) Molecular mechanics terms for the binding of PQS-675 to ligands.

of China (Nos. 22304075, 21577057, 91643105, 21874065 and 22176085), the National Key R&D Program of China (No. 2021YFF0600800).

Declaration of competing interests

The authors declare that they have no known competing financial interests or personal relationships that could have appeared to influence the work reported in this paper.

Acknowledgments

We are grateful to the High Performance Computing Center of Nanjing University for doing the numerical calculations in this paper on its blade cluster system.

Appendix A. Supplementary data

Supplementary data to this article can be found online at https://doi.org/10.1016/j.aca.2026.346110.

Data availability

Data will be made available on request.

References

[1] M. Gellert, M.N. Lipsett, D.R. Davies, Helix formation by guanylic acid, Proc. Natl. Acad. Sci. U. S. A. 48 (12) (1962) 2013–2018, https://doi.org/10.1073/pnas.48.12.2013.

[2] R. Perrone, M. Nadai, I. Frasson, J.A. Poe, E. Butovskaya, T.E. Smithgall, M. Palumbo, G. Palù, S.N. Richter, A dynamic G-quadruplex region regulates the HIV-1 long terminal repeat promoter, J. Med. Chem. 56 (16) (2013) 6521–6530, https://doi.org/10.1021/jm400914r.

[3] S. Kumar, R.K. Reddy Sannapureddi, C.S. Todankar, R. Ramanathan, A. Biswas, B. Sathyamoorthy, P.I. Pradeepkumar, Bisindolylmaleimide ligands stabilize c-MYC G-quadruplex DNA structure and downregulate gene expression, Biochemistry 61 (11) (2022) 1064–1076, https://doi.org/10.1021/acs.biochem.2c00116.

[4] P. Soldà Frasson, M. Nadai, M. Tassinari, M. Scalabrin, V. Gokhale, L.H. Hurley, S. N. Richter, Quindoline-derivatives display potent G-quadruplex-mediated antiviral activity against herpes simplex virus 1, Antivir. Res. 208 (2022) 105432, https://doi.org/10.1016/j.antiviral.2022.105432.

[5] I. Frasson, M. Nadai, S.N. Richter, Conserved G-quadruplexes regulate the immediate early promoters of human alphaherpesviruses, Molecules 24 (13) (2019) 2375, https://doi.org/10.3390/molecules24132375.

[6] A. Madireddy, P. Purushothaman, C.P. Loosbroock, E.S. Robertson, C. L. Schildkraut, S.C. Verma, G-quadruplex-interacting compounds alter latent DNA replication and episomal persistence of KSHV, Nucleic Acids Res. 44 (8) (2016) 3675–3694, https://doi.org/10.1093/nar/gkw038.

[7] L.-W. Shen, M.-Q. Qian, K. Yu, S. Narva, F. Yu, Y.-L. Wu, W. Zhang, Inhibition of Influenza A virus propagation by benzoselenoxanthenes stabilizing TMPRSS2 gene G-quadruplex and hence down-regulating TMPRSS2 expression, Sci. Rep. 10 (1) (2020) 7635, https://doi.org/10.1038/s41598-020-64368-8.

[8] A.E. Gorbalenya, S.C. Baker, R.S. Baric, R.J. de Groot, C. Drosten, A.A. Gulyaeva, B. L. Haagmans, C. Lauber, A.M. Leontovich, B.W. Neuman, D. Penzar, S. Perlman, L. L.M. Poon, D.V. Samborskiy, I.A. Sidorov, I. Sola, J. Ziebuhr, The species severe acute respiratory syndrome-related coronavirus: classifying 2019-nCoV and naming it SARS-CoV-2, Nat. Microbiol. 5 (4) (2020) 536–544, https://doi.org/10.1038/s41564-020-0695-z.

[9] O. Doluca, G4Catchall: a G-quadruplex prediction approach considering atypical features, J. Theor. Biol. 463 (2019) 92–98, https://doi.org/10.1016/j.jtbi.2018.12.007.

[10] J. Hon, T. Martínek, J. Zendulka, M. Lexa, Pqsfinder: an exhaustive and imperfection-tolerant search tool for potential quadruplex-forming sequences in R, Bioinformatics 33 (21) (2017) 3373–3379, https://doi.org/10.1093/bioinformatics/btx413.

[11] O. Kikin, L. D'Antonio, P.S. Bagga, QGRS mapper: a web-based server for predicting G-quadruplexes in nucleotide sequences, Nucleic Acids Res. 34 (2006) W676–W682, https://doi.org/10.1093/nar/gkl253.

[12] R. Zhang, K. Xiao, Y. Gu, H. Liu, X. Sun, Whole genome identification of potential G-quadruplexes and analysis of the G-quadruplex binding domain for SARS-CoV-2, Front. Genet. 11 (2020), https://doi.org/10.3389/fgene.2020.587829.

[13] D. Ji, M. Juhas, C.M. Tsang, C.K. Kwok, Y. Li, Y. Zhang, Discovery of G-quadruplex-forming sequences in SARS-CoV-2, Brief. Bioinform. 22 (2) (2021) 1150–1160, https://doi.org/10.1093/bib/bbaa114.

[14] C. Zhao, G. Qin, J. Niu, Z. Wang, C. Wang, J. Ren, X. Qu, Targeting RNA G-Quadruplex in SARS-CoV-2: a promising therapeutic target for COVID-19? Angew. Chem. Int. Ed. 60 (1) (2021) 432–438, https://doi.org/10.1002/anie.202011419.

[15] M. Hoffmann, H. Kleine-Weber, S. Schroeder, N. Krüger, T. Herrler, S. Erichsen, T. S. Schiergens, G. Herrler, N.-H. Wu, A. Nitsche, M.A. Müller, C. Drosten, S. Pöhlmann, SARS-CoV-2 cell entry depends on ACE2 and TMPRSS2 and is blocked by a clinically proven protease inhibitor, Cell 181 (2) (2020) 271–280, https://doi.org/10.1016/j.cell.2020.02.052.

[16] S. Wang, Z. Qiu, Y. Hou, X. Deng, W. Xu, T. Zheng, P. Wu, S. Xie, W. Bian, C. Zhang, Z. Sun, K. Liu, C. Shan, A. Lin, S. Jiang, Y. Xie, Q. Zhou, L. Lu, J. Huang, X. Li, AXL is a candidate receptor for SARS-CoV-2 that promotes infection of pulmonary and bronchial epithelial cells, Cell Res. 31 (2) (2021) 126–140, https://doi.org/10.1038/s41422-020-00460-y.

[17] G. Liu, W. Du, X. Sang, Q. Tong, Y. Wang, G. Chen, Y. Yuan, L. Jiang, W. Cheng, D. Liu, Y. Tian, X. Fu, RNA G-quadruplex in TMPRSS2 reduces SARS-CoV-2 infection, Nat. Commun. 13 (1) (2022) 1444, https://doi.org/10.1038/s41467-022-29135-5.

[18] H. Cui, L. Zhang, G-quadruplexes are present in human coronaviruses including SARS-CoV-2, Front. Microbiol. 11 (2020), https://doi.org/10.3389/fmicb.2020.567317.

[19] M. Bartas, V. Brázda, N. Bohálová, A. Cantara, A. Volná, T. Stachurová, K. Malachová, E.B. Jagelská, O. Porubiaková, J. Červeň, P. Pečinka, In-depth bioinformatic analyses of Nidovirales including human SARS-CoV-2, SARS-CoV, MERS-CoV viruses suggest important roles of non-canonical nucleic acid structures in their lifecycles, Front. Microbiol. 11 (2020), https://doi.org/10.3389/fmicb.2020.01583.

[20] A.K. Maiti, Identification of G-quadruplex DNA sequences in SARS-CoV2, Immunogenetics 74 (5) (2022) 455–463, https://doi.org/10.1007/s00251-022-01257-6.

[21] X.-X. Lang, Q.-Q. Yu, H.-Y. Li, Y. Luo, X.-F. Yu, H.-J. Wang, M.-Q. Wang, Identification of a non-planar imidazole-cored small molecule for selective telomeric G4 DNA targeting, Dyes Pigments 197 (2022) 109901, https://doi.org/10.1016/j.dyepig.2021.109901.

[22] K.-B. Wang, Y. Wang, J. Dickerhoff, D. Yang, DNA G-quadruplexes as targets for natural product drug discovery, Engineering 38 (2024) 39–51, https://doi.org/10.1016/j.eng.2024.03.015.

[23] D. Luo, C. Liu, E. Muturi, Z. Hu, W. Hong, C. Gao, J. Li, H. Wei, D. Wei, H. Yang, Inhibition of SARS-CoV-2 replication in cells by G-quadruplex ligands, Med. Chem. Res. 33 (11) (2024) 2169–2179, https://doi.org/10.1007/s00044-024-03347-4.

[24] G. Qin, C.A.Q. Zhao, Y. Liu, C. Zhang, G. Yang, J. Yang, Z. Wang, C.Y. Wang, C. C. Tu, Z.D. Guo, J.S. Ren, X.G. Qu, RNA G-quadruplex formed in SARS-CoV-2 used for COVID-19 treatment in animal models, Cell Discov. 8 (1) (2022) 86, https://doi.org/10.1038/s41421-022-00450-x.

[25] Q. Tong, G. Liu, X. Sang, X. Zhu, X. Fu, C. Dou, Y. Jian, J. Zhang, S. Zou, G. Zhang, X. Du, D. Liu, S. Qi, W. Cheng, Y. Tian, X. Fu, Targeting RNA G-quadruplex with repurposed drugs blocks SARS-CoV-2 entry, PLoS Pathog. 19 (1) (2023) e1011131, https://doi.org/10.1371/journal.ppat.1011131.

[26] M. Nadai, F. Doria, I. Frasson, R. Perrone, V. Pirota, G. Bergamaschi, M. Freccero, S.N. Richter, Naphthalene diimide–tetraazacycloalkane conjugates are G-quadruplex-based HIV-1 inhibitors with a dual mode of action, ACS Infect. Dis. 10 (2024) 489–499, https://doi.org/10.1021/acsinfecdis.3c00453.

[27] J. Holoubek, K. Bednářová, J. Haviernik, I. Huvarová, Z. Dvořáková, J. Černý, M. Outlá, J. Salát, E. Konkol'ová, E. Boura, D. Růžek, M. Vorlíčková, L. Eyer, D. Renčiuk, Guanine quadruplexes in the RNA genome of the tick-borne encephalitis virus: their role as a new antiviral target and in virus biology, Nucleic Acids Res. 50 (8) (2022) 4574–4600, https://doi.org/10.1093/nar/gkac225.

[28] J. Gao, C. Liang, J. Yin, Y. Bai, D. Hu, Discovery of Palbociclib as a potent c-Myc G4 stabilizer for lung cancer treatment using molecular docking, molecular dynamics simulation, and in vitro activity evaluation, Mol. Divers. 28 (6) (2024) 3965–3977, https://doi.org/10.1007/s11030-023-10789-2.

[29] J. Carvalho, T. Santos, R. Carrilho, F. Sousa, G.F. Salgado, J.A. Queiroz, C. Cruz, Ligand screening to pre-miRNA 149 G-quadruplex investigated by molecular dynamics, J. Biomol. Struct. Dyn. 38 (2020) 2276–2286, https://doi.org/10.1080/07391102.2019.1632743.

[30] T. Goldfarb, V.K. Kodali, S. Pujar, V. Brover, B. Robbertse, C.M. Farrell, D.-H. Oh, A. Astashyn, O. Ermolaeva, D. Haddad, W. Hlavina, J. Hoffman, J.D. Jackson, V. S. Joardar, D. Kristensen, P. Masterson, K.M. McGarvey, R. McVeigh, E. Mozes, M. R. Murphy, S.S. Schafer, A. Souvorov, B. Spurrier, P.K. Strope, H. Sun, A.R. Vatsan, C. Wallin, D. Webb, J.R. Brister, E. Hatcher, A. Kimchi, W. Klimke, A. Marchler-Bauer, K.D. Pruitt, F. Thibaud-Nissen, T.D. Murphy, NCBI RefSeq: reference sequence standards through 25 years of curation and annotation, Nucleic Acids Res. 53 (D1) (2025) D243–D257, https://doi.org/10.1093/nar/gkae1038.

[31] A. Bedrat, L. Lacroix, J.-L. Mergny, Re-evaluation of G-quadruplex propensity with G4Hunter, Nucleic Acids Res. 44 (4) (2016) 1746–1759, https://doi.org/10.1093/nar/gkw006.

[32] A.R. Gruber, S.H. Bernhart, R. Lorenz, The ViennaRNA web services, in: E. Picardi (Ed.), RNA Bioinformatics, Springer, New York, NY, 2015, pp. 307–326, https://doi.org/10.1007/978-1-4939-2291-8_19.

[33] S.N. Moafinejad, B.R.H. de Aquino, M.J. Boniecki, I.P.N. Pandaranadar Jeyeram, G. Nikolaev, M. Magnus, M.A. Farsani, N.G. Badepally, T.K. Wirecki, F. Stefaniak, J.M. Bujnicki, SimRNAweb v2.0: a web server for RNA folding simulations and 3D structure modeling, with optional restraints and enhanced analysis of folding trajectories, Nucleic Acids Res. 52 (W1) (2024) W368–W373, https://doi.org/10.1093/nar/gkae356.

[34] L.P.P. Patro, A. Kumar, N. Kolimi, T. Rathinavelan, 3D-NuS: a web server for automated modeling and visualization of non-canonical 3-dimensional nucleic acid

structures, J. Mol. Biol. 429 (16) (2017) 2438–2448, https://doi.org/10.1016/j.jmb.2017.06.013.
[35] M. Zgarbová, J. Šponer, M. Otyepka, T.E.I. Cheatham, R. Galindo-Murillo, P. Jurečka, Refinement of the sugar-phosphate backbone torsion beta for AMBER force fields improves the description of Z- and B-DNA, J. Chem. Theor. Comput. 11 (12) (2015) 5723–5736, https://doi.org/10.1021/acs.jctc.5b00716.
[36] S. Páll, A. Zhmurov, P. Bauer, M. Abraham, M. Lundborg, A. Gray, B. Hess, E. Lindahl, Heterogeneous parallelization and acceleration of molecular dynamics simulations in GROMACS, J. Chem. Phys. 153 (13) (2020) 134110, https://doi.org/10.1063/5.0018516.
[37] W. Humphrey, A. Dalke, K. Schulten, VMD: visual molecular dynamics, J. Mol. Graph. 14 (1) (1996) 33–38, https://doi.org/10.1016/0263-7855(96)00018-5.
[38] Maestro, Version 10.1, Schrödinger, LLC, 2015.
[39] W.L. Jorgensen, D.S. Maxwell, J. Tirado-Rives, Development and testing of the OPLS all-atom force field on conformational energetics and properties of organic liquids, J. Am. Chem. Soc. 118 (45) (1996) 11225–11236, https://doi.org/10.1021/ja9621760.
[40] Q. Li, J.-F. Xiang, Q.-F. Yang, H.-X. Sun, A.-J. Guan, Y.-L. Tang, G4LDB: a database for discovering and studying G-quadruplex ligands, Nucleic Acids Res. 41 (D1) (2013) D1115–D1123, https://doi.org/10.1093/nar/gks1101.
[41] Y.-H. Wang, Q.-F. Yang, X. Lin, D. Chen, Z.-Y. Wang, B. Chen, H.-Y. Han, H.-D. Chen, K.-C. Cai, Q. Li, S. Yang, Y.-L. Tang, F. Li, G4LDB 2.2: a database for discovering and studying G-quadruplex and i-Motif ligands, Nucleic Acids Res. 50 (D1) (2022) D150–D160, https://doi.org/10.1093/nar/gkab952.
[42] R.A. Friesner, J.L. Banks, R.B. Murphy, T.A. Halgren, J.J. Klicic, D.T. Mainz, M. P. Repasky, E.H. Knoll, M. Shelley, J.K. Perry, D.E. Shaw, P. Francis, P.S. Shenkin, Glide: a new approach for rapid, accurate docking and scoring. 1. method and assessment of docking accuracy, J. Med. Chem. 47 (7) (2004) 1739–1749, https://doi.org/10.1021/jm0306430.
[43] T.A. Halgren, R.B. Murphy, R.A. Friesner, H.S. Beard, L.L. Frye, W.T. Pollard, J. L. Banks, Glide: a new approach for rapid, accurate docking and scoring. 2. enrichment factors in database screening, J. Med. Chem. 47 (7) (2004) 1750–1759, https://doi.org/10.1021/jm030644s.
[44] J. Wang, R.M. Wolf, J.W. Caldwell, P.A. Kollman, D.A. Case, Development and testing of a general amber force field, J. Comput. Chem. 25 (9) (2004) 1157–1174, https://doi.org/10.1002/jcc.20035.
[45] T. Lu, Sobtop, Version 1.0, 2024. (Accessed 2 May 2025).
[46] T. Darden, D. York, L. Pedersen, Particle mesh Ewald: an N·log(N) method for Ewald sums in large systems, J. Chem. Phys. 98 (12) (1993) 10089–10092, https://doi.org/10.1063/1.464397.
[47] J. Zhang, T. Wang, X. Geng, L. Liu, J. Gao, Identification of Trovafloxacin, Ozanimod, and Ozenoxacin as potent c-Myc G-quadruplex stabilizers to suppress c-Myc transcription and myeloma growth, Mol. Inf. 41 (10) (2022) 2200011, https://doi.org/10.1002/minf.202200011.
[48] B.R.I. Miller, T.D.Jr. McGee, J.M. Swails, N. Homeyer, H. Gohlke, A.E. Roitberg, MMPBSA.py: an efficient program for end-state free energy calculations, J. Chem. Theor. Comput. 8 (9) (2012) 3314–3321, https://doi.org/10.1021/ct300418h.
[49] M.S. Valdés-Tresanco, M.E. Valdés-Tresanco, P.A. Valiente, E. Moreno, gmx_MMPBSA: a new tool to perform end-state free energy calculations with GROMACS, J. Chem. Theor. Comput. 17 (10) (2021) 6281–6291, https://doi.org/10.1021/acs.jctc.1c00645.
[50] T. Miyahara, H. Nakatsuji, H. Sugiyama, Similarities and differences between RNA and DNA double-helical structures in circular dichroism spectroscopy: a SAC–CI study, J. Phys. Chem. A 120 (45) (2016) 9008–9018, https://doi.org/10.1021/acs.jpca.6b08023.
[51] N.T. Dao, R. Haselsberger, M.-E. Michel-Beyerle, A.T. Phan, Following G-quadruplex formation by its intrinsic fluorescence, FEBS Lett. 585 (24) (2011) 3969–3977, https://doi.org/10.1016/j.febslet.2011.11.004.
[52] K. Mulholland, H.-J. Sullivan, J. Garner, J. Cai, B. Chen, C. Wu, Three-dimensional structure of RNA monomeric G-quadruplex containing ALS and FTD related G4C2 repeat and its binding with TMPyP4 probed by homology modeling based on experimental constraints and molecular dynamics simulations, ACS Chem. Neurosci. 11 (1) (2020) 57–75, https://doi.org/10.1021/acschemneuro.9b00572.
[53] N.J. Paradis, A. Clark, H. Gogoj, P.M. Lakernick, T.D. Vaden, C. Wu, To probe the binding of TMPyP4 to c-MYC G-quadruplex with in water and in imidazolium-based ionic liquids using spectroscopy coupled with molecular dynamics simulations, J. Mol. Liq. 365 (2022) 120097, https://doi.org/10.1016/j.molliq.2022.120097.
[54] L.-M. Zhang, Y.-X. Cui, L.-N. Zhu, J.-Q. Chu, D.-M. Kong, Cationic porphyrins with large side arm substituents as resonance light scattering ratiometric probes for specific recognition of nucleic acid G-quadruplexes, Nucleic Acids Res. 47 (2019) 2727–2738, https://doi.org/10.1093/nar/gkz064.